Report

Current Biology

Fungal Biomineralization of Manganese as a Novel Source of Electrochemical Materials

Graphical Abstract

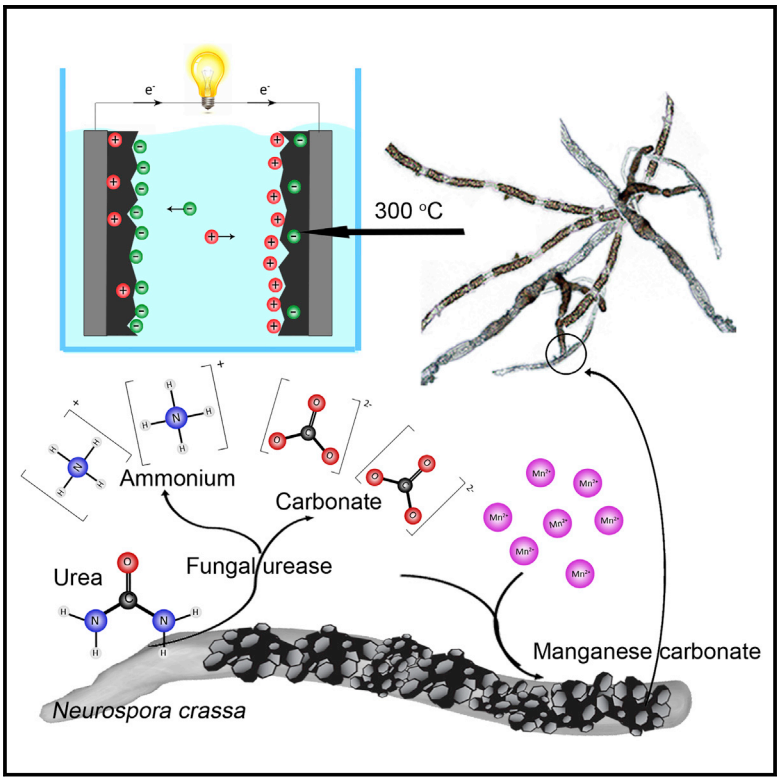

Authors

Qianwei Li, Daoqing Liu, Zheng Jia, Laszlo Csetenyi, Geoffrey Michael Gadd

Correspondence

g.m.gadd@dundee.ac.uk

In Brief

Li et al. synthesized novel electrochemical materials using a fungal Mn biomineralization process. They studied the electrochemical properties of the carbonized fungal biomass-mineral composite in a supercapacitor and a lithium-ion battery, thus providing a novel biotechnological method for preparation of sustainable electrochemical materials.

Highlights

- First synthesis of electrochemical materials from fungal Mn biomineralization is shown
- MycMnO_x/C showed a high specific capacitance (>350 F g^{-1}) in a supercapacitor
- MycMnO_x/C exhibited excellent electrochemical performance in a lithium-ion battery
- MycMnO_x/C shows significant potential for biotechnological development

Li et al., 2016, Current Biology *26*, 950–955
April 4, 2016
http://dx.doi.org/10.1016/j.cub.2016.01.068

CellPress

Current Biology
Report

Fungal Biomineralization of Manganese as a Novel Source of Electrochemical Materials

Qianwei Li,[1,5] Daoqing Liu,[2,5] Zheng Jia,[2] Laszlo Csetenyi,[3] and Geoffrey Michael Gadd[1,4,*]
[1]Geomicrobiology Group, School of Life Sciences, University of Dundee, Dundee DD1 5EH, Scotland, UK
[2]School of Chemical Engineering and Technology, Harbin Institute of Technology, Harbin 150001, People's Republic of China
[3]Concrete Technology Group, Department of Civil Engineering, University of Dundee, Dundee DD1 4HN, Scotland, UK
[4]Laboratory of Environmental Pollution and Bioremediation, Xinjiang Institute of Ecology and Geography, Chinese Academy of Sciences, Urumqi 830011, People's Republic of China
[5]Co-first author
*Correspondence: g.m.gadd@dundee.ac.uk
http://dx.doi.org/10.1016/j.cub.2016.01.068

SUMMARY

Electrical energy storage systems such as rechargeable lithium-ion batteries (LiBs) and supercapacitors have shown great promise as sustainable energy storage systems [1–4]. However, LiBs have high specific energy density (energy stored per unit mass) and act as slow, steady suppliers for large energy demands. In contrast, supercapacitors possess high specific power (energy transferred per unit mass per unit time) and can charge and discharge quickly for low energy demands. In LiBs, graphite is the most common anode material, although high electrolyte sensitivity and low charge capacity can limit performance. Efforts have been made to improve LiB or supercapacitor performance using alternative electrode materials such as carbon nanotubes and manganese oxides (Mn_xO_y) [3, 5–14]. Microorganisms play significant roles in metal and mineral biotransformations [15–22]. Fungi possess various biomineralization properties, as well as a filamentous mycelium, which may provide mechanical support for mineral deposition. Although some research has been carried out on the application of biological materials as carbon precursors [8, 9, 23], biomineralizing fungal systems have not been investigated. In this research, novel electrochemical materials have been synthesized using a fungal Mn biomineralization process based on urease-mediated Mn carbonate bioprecipitation [24]. The carbonized fungal biomass-mineral composite ($MycMnO_x/C$) showed a high specific capacitance (>350 F g^{-1}) in a supercapacitor and excellent cycling stability (>90% capacity was retained after 200 cycles) in LiBs. This is the first demonstration of the synthesis of electrode materials using a fungal biomineralization process, thus providing a novel strategy for the preparation of sustainable electrochemical materials.

RESULTS

Mineral Precipitation by *N. crassa* Grown in Urea- and $MnCl_2$-Amended Media

After 12 days of incubation in media amended with 330 mM urea and 5 mM $MnCl_2$, *N. crassa* biomass was examined by scanning electron microscopy (Figures 1A–1F). It was found that most of the hyphae became biomineralized and/or were enveloped by minerals in various formations. Figure 1D shows a cross-section of a hypha that was completely wrapped by a biomineral sheath (~2–3 μm), forming a hollow biomineralized column. Three main types of mineral formation could be observed: acicular (Figures 1A and 1B), which clustered together with the hyphae (Figure 1A); lamellar (Figures 1D, 1E, and 1F), which enveloped the hyphae as a biomineralized sheath (Figures 1D and 1E); and granular (Figures 1C, 1E, and 1F), which were mainly associated with hyphal surfaces or the other lamellar minerals. Energy-dispersive X-ray analysis (EDXA) showed that the main elements present in these minerals were Mn, P, O, and C (inset, Figure 1A). X-ray diffraction (XRD) analysis revealed that six different Mn-containing minerals were present: rhodochrosite ($MnCO_3$), switzerite ($(Mn, Fe)_3(PO_4)_2$), bixbyite ($(Mn, Fe)_2O_3$), hausmannite ($Mn^{2+}Mn^{4+}{}_2O_4$), pyrolusite (MnO_2), and manganosite (MnO) (Figure 2A).

After treatment at high temperature (300°C) for 4 hr, the biomass was carbonized, although the overall morphology did not show significant alteration (Figures 1A and 1G). The carbonized hyphae were in a biomineralized form but appeared to be more fragile. Compared with the extensive mineral deposition shown in Figure 1D, the heat-treated minerals around the hyphae became looser in their structure (Figure 1I), which may be due to the carbonization of the biomass and also to the decomposition of carbonate minerals at high temperature. Only lamellar minerals were observed (Figures 1G–1I), and the thickness of these nanoscale minerals was around 20 nm. The main elements detected were still Mn, P, O, and C (inset, Figure 1G), but XRD showed that most minerals were amorphous, which inhibited precise mineral identification. Fourier transform infrared spectroscopy (FTIR) was therefore used in an attempt to characterize these amorphous precipitates (Figure 2B). According to FTIR, no carbonate-related peaks were detected in the sample, with the peaks in the regions of 1,025 cm^{-1} and 588 cm^{-1} being due to the ν_3 and ν_4 vibrational modes of PO_4^{3-}. Taken together, these

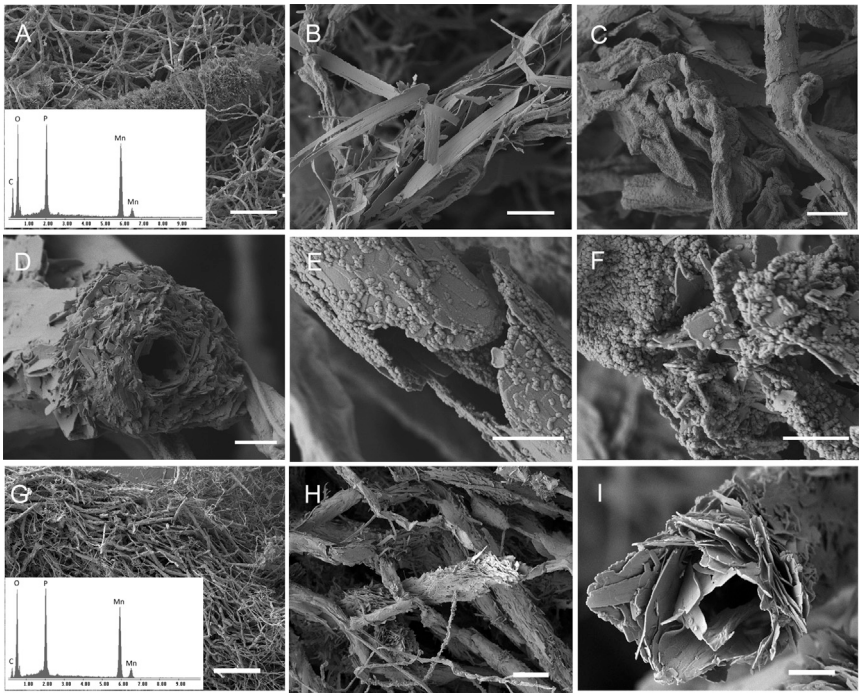

Figure 1. Scanning Electron Microscopy of *N. crassa* Incubated in Liquid Media Amended with 330 mM Urea and 5 mM $MnCl_2$

Images are before (A–F) and after (G–I) heat treatment at 300°C for 4 hr. Insets show energy-dispersive X-ray analysis (EDXA) of the minerals precipitated by *N. crassa* before (A) and after (G) the heat treatment. Scale bars, 50 μm (A), 5 μm (B and C), 2 μm (D, E, F, and I), 100 μm (G), and 10 μm (H). All samples were incubated for 12 days at 25°C in the dark. Typical images are shown from many similar examples.

EDXA (inset Figure 1G) and FTIR results (Figure 2B) therefore indicate that the amorphous minerals left after heat treatment comprised manganese phosphate and manganese oxides (MnO_X), with the valency of Mn in the mineral necessitating identification by X-ray photoelectron spectroscopy (XPS) (Figure 3).

XPS was employed to determine the surface chemical properties of the sample, and the fully scanned spectrum of the sample showed three main peaks, at 283.2 eV, 530.2 eV, and 640.5 eV, corresponding to C 1s, O 1s, and Mn 2p, respectively (Figure 3). The minor peaks located at 132.0 and 398.0 eV are assigned to P 2p and N 1s, respectively, with the phosphorus and nitrogen mainly arising from the phosphate and ammonium present in the medium (Figure 3A). The asymmetric Mn $2p_{3/2}$ main peak is found at 640.5 eV with a $2p_{3/2}$ to $2p_{1/2}$ splitting of 11.9 eV (Figure 3B), which is in accordance with previous data for Mn $2p_{3/2}$ and Mn $2p_{1/2}$ in MnO and Mn_2O_3 [25–28]. The fitted multiplet structure of Mn $2p_{3/2}$ and Mn $2p_{1/2}$ with binding energies of 644.6 eV and 656.8 eV (Figure 3B), respectively, is related to the binding energy of Mn^{4+} in MnO_2 [25]. After carbonization, some MnO_x was anchored to the surface of the carbonized mycelium. Due to the poor conductivity of the carbonized mycelium, the C-C peak shifted to 283.2 eV [29]. In addition, C-O/C-O-C and O-C=O were observed at 286.7 eV and 290 eV, respectively; partial thermal decomposition of the carbonized mycelium and manganese carbonate may contribute to these peaks. Figure 3D shows the O 1s photoemission spectra of the prepared Mn-containing sample. The spectrum was deconvoluted into three contributions with binding energies of 527.9 eV, 530.1 eV, and 532.6 eV (Figure 3D). The first two lines can be attributed to oxygen atoms bound to manganese atoms in higher and lower oxidation states (527.9 eV and 530.2 eV) as represented by Mn-O-Mn and Mn-O-H bond configurations, which correspond to the Mn(IV) in MnO_2, Mn(II) in MnO, and/or Mn(III) in Mn_2O_3, respectively [25, 26, 30]. The latter peak is assigned to oxygen from water molecules (H-O-H bonds). These results indicate that manganese atoms in lower Mn(II) oxidation states occupy a large proportion of the sample.

Electrochemical Properties of the $MycMnO_x$/C Electrode in a Supercapacitor

The electrochemical characteristics of $MycMnO_x$/C were investigated using an asymmetrical hybrid supercapacitor. There were large differences in current densities between the two electrolytes at a scan rate of 10 mV s^{-1} (Figure 4A), which were due to the electrode material ($MycMnO_x$/C) being unstable in alkaline conditions and easily performing redox reactions. According to Figure 4B, at a scan rate of 10 mV s^{-1}, the specific capacitance of $MycMnO_x$/C in KOH was 483 F g^{-1}, whereas in Na_2SO_4 it was 119 F g^{-1}. If the scan rate was increased to 500 mV s^{-1}, the specific capacitance decreased to 244.5 F g^{-1} and 38 F g^{-1}, respectively. This may be because the hyphae could facilitate the dispersion of the electrolyte ions which could then better react with the active sites. When the $MycMnO_x$/C electrode was charged at 1 A g^{-1} current density in 5.4 M KOH, a voltage plateau was observed around 0.3 V, which corresponded to the redox peak in the positive scanning cyclic voltammetry (CV) curve (Figure 4C). Reversibility, stability, and a long cycle life at high current densities are essential for practical applications of supercapacitors. Therefore, the $MycMnO_x$/C electrode was tested at 1 A g^{-1} for 200 cycles, and the initial capacity of $MycMnO_x$/C in 5.4 M KOH was 362 F g^{-1} (Figure 4D; see also Table S1). During the discharge cycling test, the capacitance retention of the electrode was 36.7% in 5.4 M KOH and 98.5% in 1 M Na_2SO_4 after 200 cycles (Figure 4D).

Electrochemical Properties of the $MycMnO_x$/C Electrode in a Lithium-Ion Battery

The electrochemical lithium storage capability of $MycMnO_x$ as an anode material in lithium-ion batteries was evaluated by assembly of CR2025 coin-type cells. Figure 4E shows CV curves at a scan rate of 0.5 mV s^{-1}. During the first cathode cycle, the sharp reduction peak close to 0.1 V corresponded to reduction of MnO_x to Mn^0 and the formation of Li_2O and the solid electrolyte interface (SEI) [31, 32]. In addition, two small peaks and one broad peak appeared around 1.4, 0.8, and 0.5 $MycMnO_x$/C,

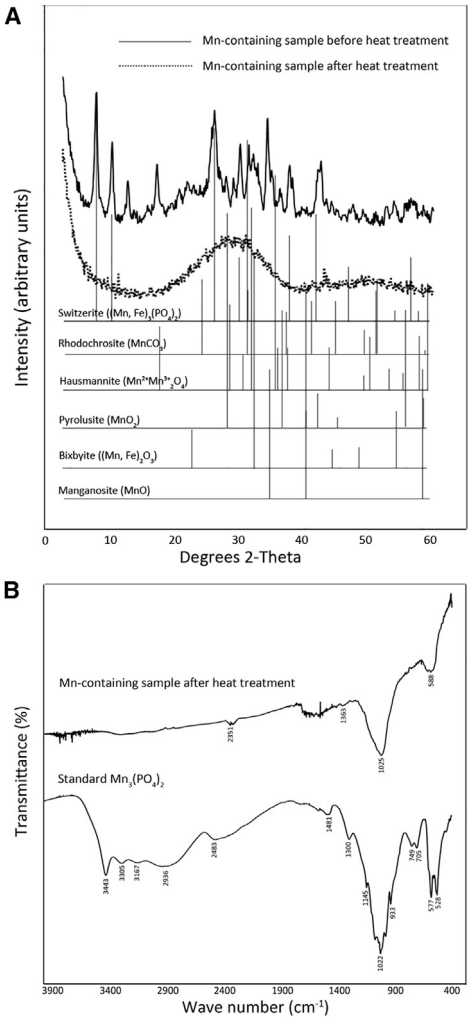

Figure 2. Identification of Minerals Precipitated by *N. crassa* Grown for 12 Days at 25°C in the Dark in Liquid Media Amended with 330 mM Urea and 5 mM $MnCl_2$

X-ray diffraction (XRD) analysis (A) and Fourier transform infrared spectroscopy (FTIR; B) of minerals precipitated by *N. crassa* after heat treatment at 300°C for 4 hr. Typical spectra are shown from one of several determinations.

which can be attributed to the reduction of $MycMnO_x$/C from a higher to a lower oxidation state and electrolyte decomposition, respectively. It is worth noting that the pair of redox peaks for MnO_x/C at 0.6 and 1.8 V stabilized after the first cycle. This phenomenon occurred in the amorphous $MycMnO_x$/C electrode in the lithium-ion battery, which means that the Mn(II) in amorphous $MycMnO_x$/C could be re-oxidized to a higher oxidation state. The conversion reaction may be written as follows:

$$MnO_x + 2xLi \leftrightarrow Mn + xLi_2O$$

The charge/discharge curves of the $MycMnO_x$/C battery at a current density of 0.1 A g^{-1} between 0.01 and 3 V are shown in Figure 4F. During the first discharge process, a sustained voltage plateau at 0.5 V was observed, which was attributed to the reduction of MnO_x to Mn^0 [33] and which then decreased gradually to 0.01 V, delivering a discharge capacity of 911 mA h g^{-1}. In the subsequent cycling process, the discharge plateau increased to about 1.0 V, which could be partially related to the improved kinetics of the reactants which consume less energy to be activated after the first discharge process [33, 34]. The initial columbic efficiency was 46.7%. The irreversible capacity in the first few cycles could be mainly due to the large capacity loss in the first cycle, which was mainly attributed to the formation of a SEI layer due to chemical reactions between electrolyte and the anode material.

For further investigation of the electrochemical performance of the $MycMnO_x$/C hybrid, the rate capability of the sample was tested (Figure 4G). The reversible capacity of $MycMnO_x$/C was around 400 mA h g^{-1} over the first few cycles at a current density of 100 mA h g^{-1}. When the current density reached 0.5 A g^{-1}, the specific capacity of the $MycMnO_x$/C hybrid still remained about 200 mA h g^{-1} (Figure 4G). Figure 4H shows the discharge/charge cycling performance of the $MycMnO_x$/C hybrid at a current density of 100 mA g^{-1} for 200 cycles. It is interesting to find that the reversible capacity dropped slowly over the first 50 cycles and then increased with cycling and remained at 92% of its initial specific capacity after 200 cycles (see also Table S2). It has been reported that electrolyte degradation will result in the formation of a polymeric gel-like film around $MycMnO_x$ particles, and growth of this polymeric layer will increase the capacity of the metal oxide with further cycling [35].

DISCUSSION

Much research has been carried out on the synthesis of advanced materials, using a biological template, with nano- or microscale structures and unique properties [11, 23]. Compared to conventional methods, minerals precipitated by a biomineralization process may contain an inorganic/organic hierarchical structure, which can show excellent physico-chemical attributes and biological properties [36]. In this work, we have focused on the synthesis of MnO_x by a fungal biomineralization system and have investigated its potential application as an electrode material in supercapacitors and lithium-ion batteries.

Previous research has demonstrated that the urease-positive fungus *Neurospora crassa* is an excellent candidate for $CaCO_3$ biomineralization, and more than 90% of supplied calcium (50 mM) could be precipitated as calcite [24]. Such performance of ureolytic fungi in urea-supplemented media suggested a useful method for the synthesis of calcite, as well as other metal-containing carbonates. For example, ~50% of supplied $CdCl_2$ (0.5 M) was precipitated as pure otavite ($CdCO_3$) by the culture supernatant obtained after growth of *N. crassa* in urea-supplemented medium [24]. Other urease-positive fungi (*Pestalotiopsis* sp. and *Myrothecium gramineum*) isolated from calcareous soil were also found to be able to precipitate $CaCO_3$ and $SrCO_3$, as well as olekminskite ($Sr(Sr, Ca)(CO_3)_2$) and Sr-containing vaterite ($(Ca_xSr_{1-x})CO_3$) [21]. In this work, *N. crassa* was cultured in urea- and $MnCl_2$-modified media, various mineral morphologies were observed to be accreted around the hyphae, and $MnCO_3$ was identified by XRD. With thermal treatment of the biomass-mineral composite at 300°C for 4 hr, MnO_x containing different oxidation states of Mn resulted and the fungal biomass was carbonized to provide a coal-like material that was used as a carbon precursor. Other ureolytic fungi could also be used in this type of approach.

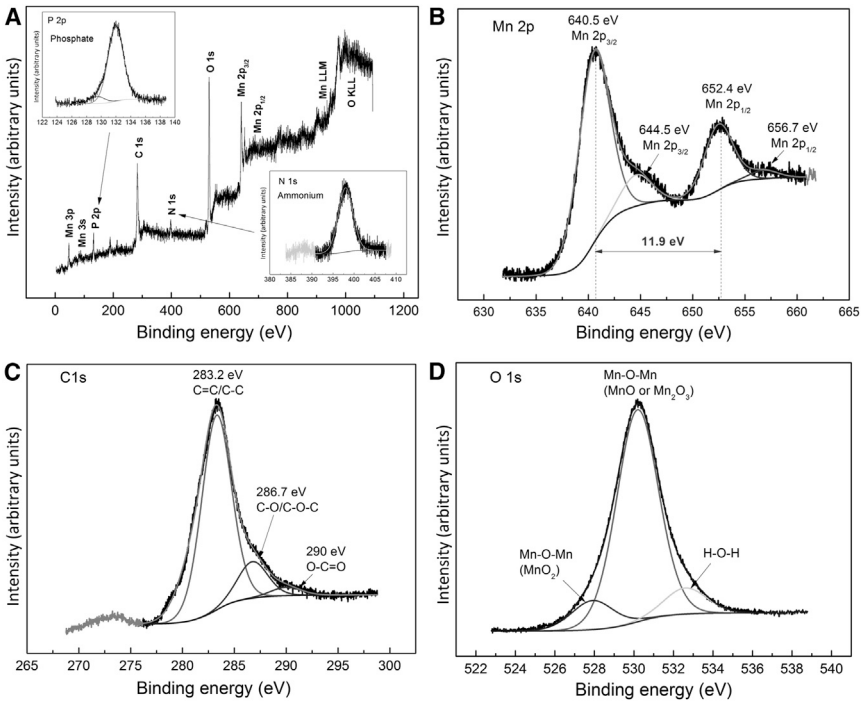

Figure 3. X-Ray Photoelectron Spectroscopy of Carbonized Fungal Biomass with Mn-Containing Minerals

(A) Total X-ray photoelectron spectroscopy (XPS) spectra. Insets show the XPS spectra of N 1s and P 2p, respectively. The spectral peaks contributing to the spectrum are labeled and the near-horizontal line is the background. The jagged line is the raw spectra data, and the smooth curve is the best fit spectrum.

(B–D) XPS Mn 2p (B), C 1s (C), and O 1s (D) spectra. Symbols and curves are as in (A). Typical spectra are shown from one of several determinations.

Biological materials, such as biomass from fungi [8, 11, 12], microalgae [9, 14], or bacteria [23], have been used previously as sustainable carbon precursors for energy storage devices [36]. Long et al. [12] obtained a porous layered carbonaceous material from hydrothermally treated fungal biomass that possessed a high surface area, bulk density, and a multilayer cross-linked framework. When used as an electrode material in supercapacitors, it showed a high volumetric capacitance and excellent cycling stability. Due to rapid and reversible redox reactions between the different oxidation states, theoretical high energy storage capacity, and low cost, MnO_x has been used as an electrode material in supercapacitors [29, 37], lithium-ion batteries [38, 39], and lithium-air batteries [39]. However, pure MnO_x has poor electronic conductivity, and it exhibits a rapid decrease in storage capacity of Li^+ and ion diffusion during the charge/discharge processes [38]. Many efforts have been made in an attempt to solve these problems, such as using conductive additives and carbon coatings [38]. Reddy et al. [38] combined coaxial MnO_2 nanotubes with conducting carbon nanotubes (CNTs) to improve the performance of lithium-ion batteries and showed that such MnO_2/CNT hybrid nanotubes enhanced the electronic conductivity and reversible capacity of the electrode. For improvement of the energy and power density of a supercapacitor, bacterial-cellulose-derived carbon nanofibers loaded with MnO_2 were used as the anode, and this cost-effective device delivered a high energy density (32.91 W h kg^{-1}) and excellent cycling stability after 2,000 cycles [40].

Though much research has been carried out on the synthesis or capability enhancement of electrode materials, little attention has been paid to the construction of novel electrode materials using fungal biomineralization products. After thermal treatment, the MycMnO_x derived from thermal decomposition of the biomineralized $MnCO_3$ comprised an outer shell with the conducting carbonized fungal biomass in the inner core. Compared with conventional physico-chemical methods, our experiments illustrate a facile and novel procedure for preparation of MycMnO_x/C materials. The biomineralization process of $MnCO_3$ by a ureolytic fungus provides not only the carbon precursor, but also a source of MnO_x, which can be used directly as an electrode material after heat treatment. When used as an electrode material in a supercapacitor, compared with MnO_x synthesized by other methods, MycMnO_x/C exhibited a good specific capacitance of 362 F g^{-1} at a current density of 1 A g^{-1} (see also Table S1). The fungal mycelium provides a framework for the deposition of minerals and also evenly distributes the electrolyte ions, facilitating redox reactions in solution and thus providing an advantage over, e.g., a bacterial system. Compared with other reported MnO_x materials in lithium-ion batteries (see also Table S2), MycMnO_x/C did not show a very good capacity (~400 mA h g^{-1}) at a current density of 100 mA g^{-1}, which might be due to the low concentration of Mn^{2+} added to the medium. However, it is worth noting that MycMnO_x/C had an outstanding cycling stability and 91% of capacity was retained after 200 cycles. According to XRD analysis, most of the decomposed minerals derived from fungal bioprecipitation were amorphous, although some were present in nanoscale sheets. Compared with crystalline MnO_x/C, the amorphous MycMnO_x/C nanosheets had a lower volume change during the redox reactions, and this could also enhance the structural stability of MycMnO_x/C. During the process of biomineralization, the hyphae provide a template for nucleation, growth, and deposition of minerals, and the thermal decomposition of the biogenic $MnCO_3$ and carbonization of fungal biomass result in a large specific surface area of MycMnO_x/C. This is the first report of the application of fungal-derived MnO_x as an electrode material in supercapacitors and lithium-ion batteries, with MycMnO_x/C showing good electrochemical properties, especially in cycling stability in lithium-ion batteries. Fungal biomineralization methods for the synthesis of mycogenic MnO_x/C could therefore be a useful alternative strategy for the preparation of novel electrochemical materials.

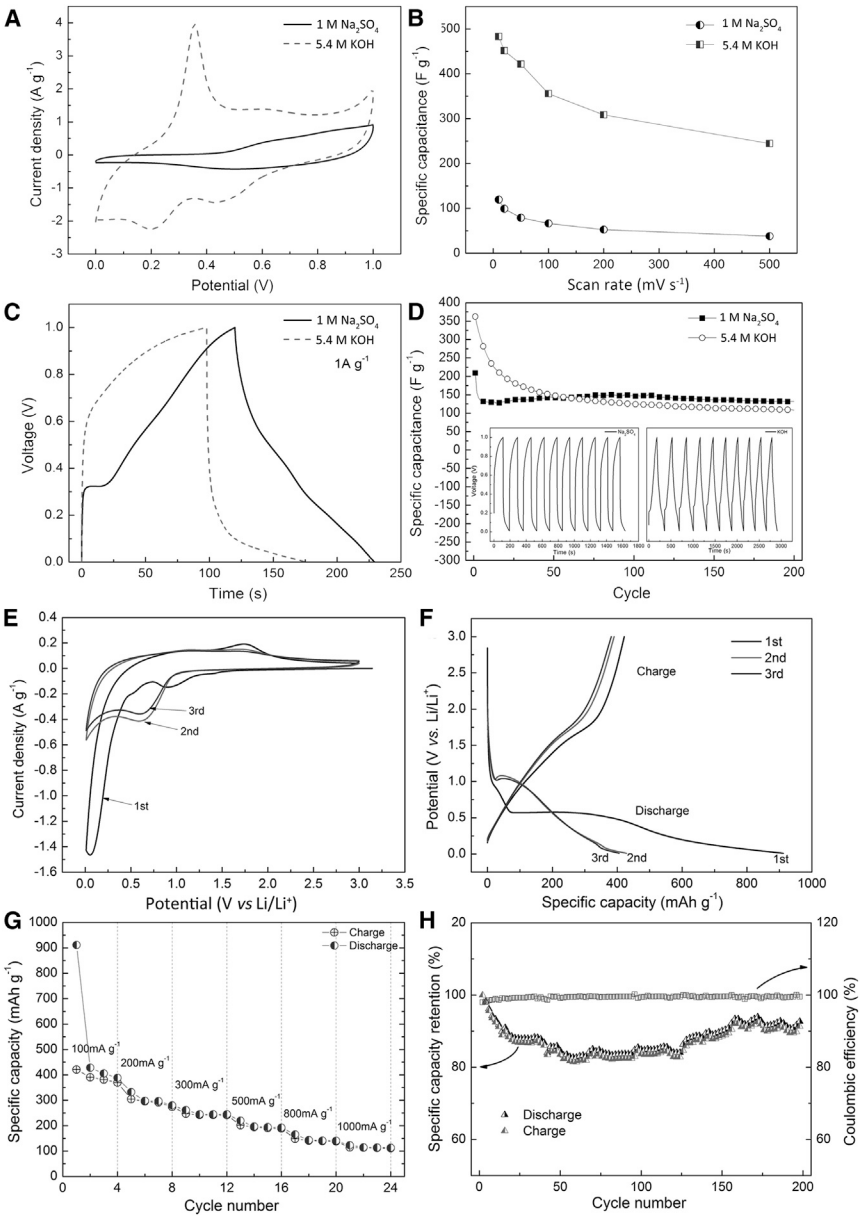

Figure 4. Electrochemical Measurements of a MycMnO$_x$/C Electrode in a Supercapacitor and Lithium-Ion Battery

(A–D) Supercapacitor. Cyclic voltammetry (CV) curves (A), specific capacitances at various scan rates in different electrolytes (B), galvanostatic charge/discharge curves of MycMnO$_x$/C with 1 A g^{-1} current density in an electrolyte of 5.4 M KOH and 1 M Na_2SO_4 after 20 cycles (C), and cycling performance of biomass material electrode at a current density of 1 A g^{-1} for 200 cycles (D) are shown. The inset shows the first 10 charge/discharge cycles.

(E–H) Lithium-ion battery. Cyclic voltammetry (CV) curves at a scan rate of 0.5 mV/s (E), charge/discharge curves at 0.1 A g^{-1} (F), charge/discharge capacity of MycMnO$_x$/C at different current densities (G), and cycling performance and coulombic efficiency at a 0.5 A g^{-1} current density (H) are shown. Typical patterns are shown from one of several determinations.

See also Tables S1 and S2.

SUPPLEMENTAL INFORMATION

Supplemental Information includes Supplemental Experimental Procedures and two tables and can be found with this article online at http://dx.doi.org/10.1016/j.cub.2016.01.068.

AUTHOR CONTRIBUTIONS

Conceptualization, Q.L., D.L., and G.M.G.; Methodology, Q.L., D.L., L.C., and G.M.G.; Investigation, Q.L. and D.L.; Writing – Original Draft, Q.L. and D.L.; Writing – Review & Editing, Q.L. and G.M.G.; Funding Acquisition, G.M.G.; Resources, G.M.G., Z.J., and L.C.; Supervision, G.M.G.

ACKNOWLEDGMENTS

The authors gratefully acknowledge the help of Mr. Martin Kierans (Central Imaging Facility, School of Life Sciences, University of Dundee) and Dr. Yongchang Fan (Division of Physics, University of Dundee) for assistance with scanning electron microscopy, Mrs. Sylvia Williamson (School of Chemistry, University of St Andrews) and Dr. Aida Fuente Cuesta (School of Chemistry, University of St Andrews) for assistance with Fourier transform infrared spectrometry, and Dr. Stephen Francis (School of Chemistry, University of St Andrews) for assistance with X-ray photoelectron spectroscopy. We also acknowledge financial support from the China Scholarship Council through a PhD scholarship to Q.L. (no. 201206120066). G.M.G. gratefully acknowledges an award under the 1000 Talents Plan with the Xinjiang Institute of Ecology and Geography, Chinese Academy of Sciences, Urumqi, China.

Received: December 23, 2015
Revised: January 27, 2016
Accepted: January 27, 2016
Published: March 17, 2016

REFERENCES

1. Simon, P., and Gogotsi, Y. (2008). Materials for electrochemical capacitors. Nat. Mater. 7, 845–854.

2. Ji, L., Lin, Z., Alcoutlabi, M., and Zhang, X. (2011). Recent developments in nanostructured anode materials for rechargeable lithium-ion batteries. Energy Environ. Sci. *4*, 2682–2699.
3. Liu, J., Zhang, J., Yang, Z., Lemmon, J.P., Imhoff, C., Graff, G.L., Li, Li., Hu, J., Wang, C., Xiao, J., et al. (2013). Materials science and materials chemistry for large scale electrochemical energy storage: from transportation to electrical grid. Adv. Funct. Mater. *23*, 929–946.
4. Ding, J., Wang, H., Li, Z., Cui, K., Karpuzov, D., Tan, X., Kohandehghan, A., and Mitlin, D. (2015). Peanut shell hybrid sodium ion capacitor with extreme energy-power rivals lithium ion capacitors. Energy Environ. Sci. *8*, 941–955.
5. Nakayama, M., Kanaya, T., and Inoue, R. (2007). Anodic deposition of layered manganese oxide into a colloidal crystal template for electrochemical supercapacitor. Electrochem. Commun. *9*, 1154–1158.
6. Sharma, R.K., Oh, H.S., Shul, Y.G., and Kim, H. (2007). Carbon-supported, nano-structured, manganese oxide composite electrode for electrochemical supercapacitor. J. Power Sources *173*, 1024–1028.
7. Ma, S.B., Nam, K.W., Yoon, W.S., Yang, X., Ahn, K.Y., Oh, K.H., and Kim, K.B. (2007). A novel concept of hybrid capacitor based on manganese oxide materials. Electrochem. Commun. *9*, 2807–2811.
8. Zhu, H., Wang, X., Yang, F., and Yang, X. (2011). Promising carbons for supercapacitors derived from fungi. Adv. Mater. *23*, 2745–2748.
9. Falco, C., Sevilla, M., White, R.J., Rothe, R., and Titirici, M.M. (2012). Renewable nitrogen-doped hydrothermal carbons derived from microalgae. ChemSusChem *5*, 1834–1840.
10. Zhang, X., Zhang, X., He, W., Yue, Y., Liu, H., and Ma, J. (2012). Biocarbon-coated LiFePO4 nucleus nanoparticles enhancing electrochemical performances. Chem. Commun. (Camb.) *48*, 10093–10095.
11. Sun, H., He, W., Zong, C., and Lu, L. (2013). Template-free synthesis of renewable macroporous carbon via yeast cells for high-performance supercapacitor electrode materials. ACS Appl. Mater. Interfaces *5*, 2261–2268.
12. Long, C., Chen, X., Jiang, L., Zhi, L., and Fan, Z. (2015). Porous layer-stacking carbon derived from in-built template in biomass for high volumetric performance supercapacitors. Nano Energy *12*, 141–151.
13. Pol, V.G., and Thackeray, M.M. (2011). Spherical carbon particles and carbon nanotubes prepared by autogenic reactions: evaluation as anodes in lithium electrochemical cells. Energy Environ. Sci. *4*, 1904–1912.
14. Xia, Y., Xiao, Z., Dou, X., Huang, H., Lu, X., Yan, R., Gan, Y., Zhu, W., Tu, J., Zhang, W., and Tao, X. (2013). Green and facile fabrication of hollow porous MnO/C microspheres from microalgaes for lithium-ion batteries. ACS Nano *7*, 7083–7092.
15. Ehrlich, H.L. (1996). How microbes influence mineral growth and dissolution. Chem. Geol. *132*, 5–9.
16. Ehrlich, H.L., and Newman, D.K. (2009). Geomicrobiology, Fifth Edition (CRC Press/Taylor & Francis).
17. Kolo, K., Keppens, E., Préat, A., and Claeys, P. (2007). Experimental observations on fungal diagenesis of carbonate substrates. J. Geophys. Res. *112*, G01007.
18. Gadd, G.M. (2010). Metals, minerals and microbes: geomicrobiology and bioremediation. Microbiology *156*, 609–643.
19. Gadd, G.M., and Raven, J.A. (2010). Geomicrobiology of eukaryotic microorganisms. Geomicrobiol. J. *27*, 491–519.
20. Fomina, M., Burford, E.P., Hillier, S., Kierans, M., and Gadd, G.M. (2010). Rock-building fungi. Geomicrobiol. J. *27*, 624–629.
21. Li, Q., Csetenyi, L., Paton, G.I., and Gadd, G.M. (2015). $CaCO_3$ and $SrCO_3$ bioprecipitation by fungi isolated from calcareous soil. Environ. Microbiol. *17*, 3082–3097.
22. Gadd, G.M. (2009). Biosorption: critical review of scientific rationale, environmental importance and significance for pollution treatment. J. Chem. Technol. Biotechnol. *84*, 13–28.
23. Shim, H.W., Jin, Y.H., Seo, S.D., Lee, S.H., and Kim, D.W. (2011). Highly reversible lithium storage in *Bacillus subtilis*-directed porous Co_3O_4 nanostructures. ACS Nano *5*, 443–449.
24. Li, Q., Csetenyi, L., and Gadd, G.M. (2014). Biomineralization of metal carbonates by *Neurospora crassa*. Environ. Sci. Technol. *48*, 14409–14416.
25. Strohmeier, B.R., and Hercules, D.M. (1984). Surface spectroscopic characterization of manganese/aluminum oxide catalysts. J. Phys. Chem. *88*, 4922–4929.
26. Toupin, M., Brousse, T., and Bélanger, D. (2004). Charge storage mechanism of MnO_2 electrode used in aqueous electrochemical capacitor. Chem. Mater. *16*, 3184–3190.
27. Biesinger, M.C., Payne, B.P., Grosvenor, A.P., Lau, L.W.M., Gerson, A.R., and Smart, R.S.C. (2011). Resolving surface chemical states in XPS analysis of first row transition metals, oxides and hydroxides: Cr, Mn, Fe, Co and Ni. Appl. Surf. Sci. *257*, 2717–2730.
28. Lu, X., Zheng, D., Zhai, T., Liu, Z., Huang, Y., Xie, S., and Tong, Y. (2011). Facile synthesis of large-area manganese oxide nanorod arrays as a high-performance electrochemical supercapacitor. Energy Environ. Sci. *4*, 2915–2921.
29. Dilsiz, N., and Wightman, J.P. (2000). Effect of acid–base properties of unsized and sized carbon fibers on fiber/epoxy matrix adhesion. Colloids Surf. A Physicochem. Eng. Asp. *164*, 325–336.
30. Sopčić, S., Peter, R., Petravić, M., and Mandić, Z. (2013). New insights into the mechanism of pseudocapacitance deterioration in electrodeposited MnO_2 under negative potentials. J. Power Sources *240*, 252–257.
31. Li, X., Li, D., Qiao, L., Wang, X., Sun, X., Wang, P., and He, D. (2012). Interconnected porous MnO nanoflakes for high-performance lithium ion battery anodes. J. Mater. Chem. *22*, 9189–9194.
32. Li, X., Li, D., Wei, Z., Shang, X., and He, D. (2014). Interconnected MnO_2 nanoflakes supported by 3D nanostructured stainless steel plates for lithium ion battery anodes. Electrochim. Acta *121*, 415–420.
33. Liu, Y., Zhao, X., Li, F., and Xia, D. (2011). Facile synthesis of MnO/C anode materials for lithium-ion batteries. Electrochim. Acta *56*, 6448–6452.
34. Zhong, K., Xia, X., Zhang, B., Li, H., Wang, Z., and Chen, L. (2010). MnO powder as anode active materials for lithium ion batteries. J. Power Sources *195*, 3300–3308.
35. Grugeon, S., Laruelle, S., Dupont, L., and Tarascon, J.M. (2003). An update on the reactivity of nanoparticles Co-based compounds towards Li. Solid State Sci. *5*, 895–904.
36. Ryu, J., Kim, S.W., Kang, K., and Park, C.B. (2010). Mineralization of self-assembled peptide nanofibers for rechargeable lithium ion batteries. Adv. Mater. *22*, 5537–5541.
37. Si, W., Yan, C., Chen, Y., Oswald, S., Han, L.Y., and Schmidt, O.G. (2013). On chip, all solid-state and flexible micro-supercapacitors with high performance based on MnO_x/Au multilayers. Energy Environ. Sci. *6*, 3218–3223.
38. Reddy, A.L.M., Shaijumon, M.M., Gowda, S.R., and Ajayan, P.M. (2009). Coaxial MnO_2/carbon nanotube array electrodes for high-performance lithium batteries. Nano Lett. *9*, 1002–1006.
39. Thapa, A.K., Pandit, B., Thapa, R., Luitel, T., Paudel, H.S., Sumanasekera, G., Sunkara, M.K., Gunawardhana, N., Ishihara, T., and Yoshio, M. (2014). Synthesis of mesoporous birnessite-MnO_2 composite as a cathode electrode for lithium battery. Electrochim. Acta *116*, 188–193.
40. Chen, L.F., Huang, Z.H., Liang, H.W., Guan, Q.F., and Yu, S.H. (2013). Bacterial-cellulose-derived carbon nanofiber@MnO_2 and nitrogen-doped carbon nanofiber electrode materials: an asymmetric supercapacitor with high energy and power density. Adv. Mater. *25*, 4746–4752.